GISAXS study of Si nano structures in SiO_2 matrix for solar cell applications

Branko Pivac*[1], Pavo Dubček[1], Ivana Capan[1], Hrvoje Zorc[1], Jasna Dasović[1], Sigrid Bernstorff[2], Marvin Wu[3], Branislav Vlahovic[3]

[1]R. Bošković Institute, P.O. Box 180, Zagreb, Croatia
[2]Sincrotrone Trieste, SS 14, km 163.5, Basovizza (TS), Italy
[3]North Carolina Central University, Durham, NC, USA

Received xxxx, revised xxxx, accepted ZZZ
Published online ZZZ

Keywords: Si nanostructures, SiO_x/SiO_2 superlattice, small angle X-ray scattering, photoluminescence

Corresponding author: B. Pivac, e-mail: pivac@irb.hr; phone: 385-1-4561068; fax: 385-1-4680114;

We explored Si nanoparticles formed in SiO_2 matrix suitable for advanced solar cells application. To this purpose a superstructure consisting of alternating 5 nm thick SiO_x and SiO_2 layers was deposited by high vacuum evaporation from solid sources. After high temperature annealing of such structures in high vacuum, the SiO_x decomposed and Si nanoparticles aggregated at their former position forming therefore a superstructure of Si nanoparticles embedded in dielectric SiO_2 matrix. To explore such nano-objects formation in different matrix, grazing incidence small-angle X-ray scattering (GISAXS) seems to be as relatively easy and non-destructive technique. Despite the fact that due to the rather small difference in electron density between Si and SiO_2, which makes GISAXS contrast is very small, by performing GISAXS with intense synchrotron light and subtracting the dominant surface contribution to the overall signal we managed to retrieve information on the structural changes within the layers. The conclusions from the GISAXS analysis were confirmed by photoluminescence measurements.

1 Introduction

Silicon nanoparticles embedded in suitable dielectric matrices are still intensively studied due to their suitability for all-Si tandem solar cells [1]. The target is to shift the absorption in Si nanoparticles to higher energies, as compared to bulk Si material, with help of the quantum confinement effect and to secure an efficient charge carrier transport. One of the key issues in this respect is to ensure high self-ordering without the use of sophisticated and expensive lithographical techniques. A method that was suggested [2,3], based on the superlattice formation of stacked SiO_x/SiO_2 layers, was expected to enable an efficient control of the size distribution, position and density of the produced nanocrystals. The compatibility of this method with common microelectronic device fabrication materials and techniques makes it attractive for potential applications in integrated optoelectronic devices, as well as for advanced solar cells production [4-6]. Still, the diffusion and phase separation process in such a confined geometry and complex system is not yet completely understood. To analyze the Si nanoparticles formation and their final embedded position in dielectric matrix like SiO_2 the grazing incidence small angle scattering (GISAXS) appears to be a suitable

and nondestructive technique despite the difficulty of a very small difference in electronic density between Si nanoparticles and the SiO_2 matrix.

In this paper we illustrate the analysis of structural changes in the SiO_x/SiO_2 superlattice deposited by direct physical evaporation (PVD) and the evolution of nanoparticles during subsequent annealing. This analysis is complemented with photoluminescence spectroscopy.

2 Experimental

Amorphous $SiO_x/SiO2$ superlattices were prepared by a high vacuum evaporation of alternating films of SiO_x and SiO_2 from commercially available (Balzers) solid sources. Each layer was 5 nm thick (forming a stack of 10 bilayers plus 20 nmSiO_2 capping layer) on a clean Si (100) substrate held at room temperature. Rotation of the Si substrate during evaporation ensured homogeneity during the films deposition over the whole substrate surface. After deposition, the samples were annealed at different temperatures starting from 600°C to 1100 °C for 1h in vacuum better than 10^{-6} Pa to induce the Si nanocrystals formation.

The GISAXS experiments were carried out at the synchrotron facilities of Elettra, Trieste, Italy on the SAXS beamline [7], using synchrotron radiation with wavelength λ=0.154 nm (photon energy of 8 keV). Measurements were performed at several grazing incident angles α_i in steps of 0.01º starting from the critical angle for total external reflection of the silicon substrate $\alpha_{crit}(Si) = 0.23°$. A two-dimensional CCD detector with 1024 × 1024 pixels, positioned perpendicular to the incident beam at a detector to sample distance L=2000 mm, was used to record the SAXS intensity. A thin Al-strip was placed in front of the CCD detector to avoid saturation of the detector in the specular plane direction where the usually much stronger surface scattering is present. The spectra were corrected for the background intensity and the detector response.

PL measurements were performed with the 514 nm line of an Ar ion laser. The signal was analyzed by a double grating monochromator and was detected by a photomultiplier. All spectra were measured at room temperature and were corrected for the detector response.

3 Results and discussion

In Fig. 1 a 2-D GISAXS pattern obtained from the sample annealed at 900°C is shown as an example of the procedure that will be adopted in this presentation. As the 2-D detector was placed perpendicular to the direct beam the angular positions of its pixels are given by q_y in the direction parallel to the sample surface and q_z perpendicular to it. Here $q=|\boldsymbol{q}|$ is the scattering wave vector ($q=k_f-k_i$, $q=(4\pi\sin\vartheta)/\lambda$, k_i, k_f are the wave vectors of the incident and

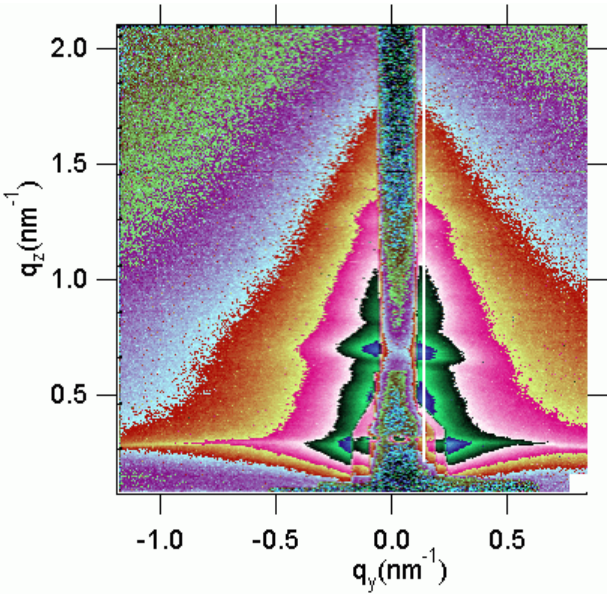

Figure 1 2-D GISAXS pattern obtained at the incident angle 0.03° above the critical angle from the sample annealed at 900°C. The white line in the figure indicates place where the line cut was made.

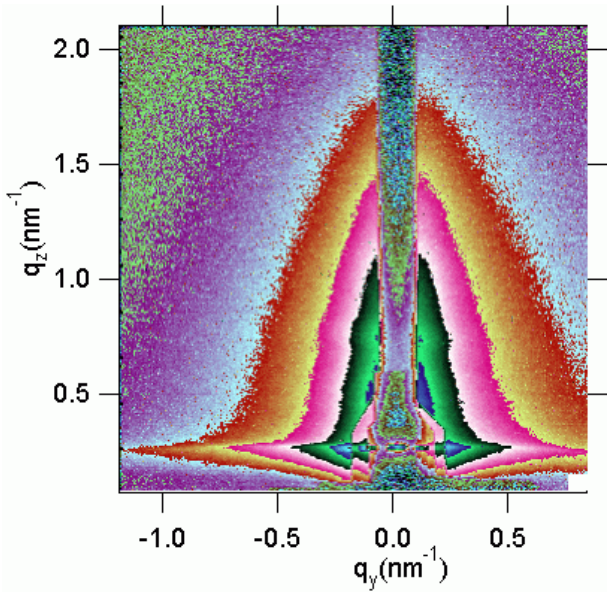

Figure 2 2-D GISAXS pattern obtained at the critical incident angle for the same sample as in Fig. 1.

scattered beams, respectively, and 2ϑ is the scattering angle).

The intensities close to the specular plane (values close to q_y=0) are reduced by the aluminium absorber necessary to protect the detector from overloading by the reflected direct beam and to gain in the signal to noise ratio in the low intensities region at the edges of the image.

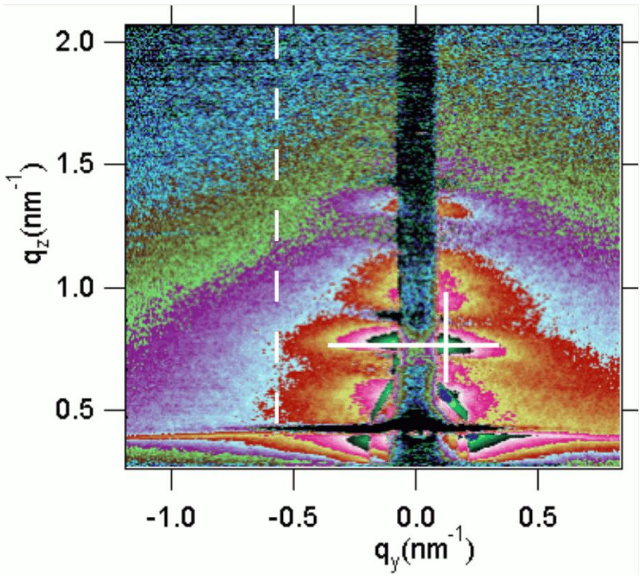

Figure 3 The difference between the intensities from Fig. 1. and Fig. 2. (see the text for details). The white full lines in the figure indicate those parts of the intensity pattern used for the analysis of the Bragg peak. The white dashed line represents the position where the intensities for the Guinier plot were taken.

The image shown in Fig. 1. was taken at 0.03° above the critical angle so that the incoming beam can penetrate the film and scattering produces information on the film structure. In that image the high intensity area at q_z=0.3 nm^{-1} corresponds to the critical angle position. Above it, at q_z=0.7 nm^{-1} there is a Bragg maximum due to the repetitive multilayer structure and a generally bell shaped scattering pattern from the sample surface is dominating the contribution to the image, overlaying valuable information from the bulk.

Fig. 2. shows the image taken at the critical angle where the beam propagates parallel to the surface and produces the information of the surface roughness. Since the penetration is very limited (typically 10-20nm) the scattering from the interior of the film is very weak. However, the difference between Figs. 1. and 2., shown in Fig. 3. reveals a different pattern. Now the surface contribution dominating in Figs. 1 and 2. is removed and the signal from the film is enhanced. The first and the second Bragg peaks, due to the repetitive structure of the multilayer film are clearly resolved at q_z=0.7 nm^{-1} and q_z=1.3 nm^{-1}. Moreover, a large hemispherical signal in the background dominates the image, clearly indicating the presence of nanoparticles in the bulk of the film.

In this approach we neglect the correlation between the surface of the film and the interfaces between the (few top) layers of the film, which can be justified by gaining the information about the nanoparticles scattering.

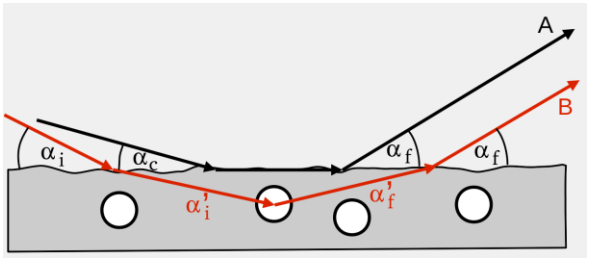

Figure 4 Schematic illustration of the experiment, where the beam marked A represents the image given in Fig. 2., i.e. the beam impinges on the sample at the critical angle α_c and propagates parallel to the rough surface. When the beam (case B) impinges at larger angle α_i than α_c the probing beam enters the bulk (containing nanoparticles of different material) with the angle $\alpha_{i'}$ different from α_i (determined by the laws of refraction) and exit with the angle α_f.

Fig. 4 shows the schematic representation of the described experiment, where the image given in Fig. 2. is equivalent to the scattering of beam A in Fig. 4. Here the beam impinges at the critical angle α_c and propagates parallel to the surface of the sample, giving therefore dominantly the information on the surface roughness. If the entering beam impinges at a higher angle, i.e. the beam B in Fig. 4., then it refracts and enters the bulk of the film probing its structure and gives the combined information as given in Fig. 1. The surface scattering is slightly different for the two cases in Fig. 4., due to the increment of the grazing angle. The intensities have been normalized with respect to the different grazing incidence angles and effects of refraction, but, since the change of angle was very small, the change of intensities of the surface scattering is neglected in the subtraction.

In Fig. 5. GISAXS intensities along q_y=0.15 nm^{-1} (parallel to the specular plane, perpendicular to the sample surface) taken at $\alpha_i = \alpha_{crit}$+0.03º are shown. At this incidence angle the penetration depth corresponds to the overall film thickness and therefore the ratio of the film to substrate scattered intensity is maximized. The specular peak is almost nonexistent here (off specular plane of analysis), and the Yoneda peak [8], which has virtually the same intensity as in the specular plane, is therefore clearly resolved at q_z=0.3 nm^{-1}. The Bragg maximum due to the re-

petitive structure is also well resolved. Moreover, the second and, at certain temperatures, the third order of the Bragg peaks are visible at q_z=1.3 nm^{-1} q_z=1.8 nm^{-1}, respectively. The relatively short in-plane correlation of the inhomogeneities within the layers results in a horizontal broadening of the Bragg peak, but these are not sharp and the structure of the peak is apparently the same for all the annealed samples below 1100ºC. However shifting of the peaks with the annealing temperatures can be still observed, since this is the consequence of a slight variation of the bilayer thickness.

The existence of the very strong intensities and multiple orders of the Bragg peaks shown in Figs. 3. and 5. indicates the presence of a strong correlation among the interface roughnesses of the different SiO_x and SiO_2 layers which persists up to very high annealing temperature (shown in Fig. 5.). To further explore this, we fitted the profiles shown in Fig. 6. by using standard formulas for correlated roughness calculated in the distorted-wave Born approximation [9]. The fitting parameters were the thicknesses of the layers (defining the Bragg peak position in vertical direction); surface roughnesses (defining the slope of the GISAXS curve); and lateral and vertical correlation lengths (defining the width of the Bragg peak). The examples of the extracted horizontal and vertical 1D experimental profiles from Fig. 3. and the corresponding fittings are shown in Fig. 6. The incidence angles were chosen to ensure maximal intensity of the signal; different values indicate changes in the refraction index of the material with annealing.

The results of the fitting are summarized in Fig. 7., which shows that there is no significant variation of the horizontal correlation (red open dots) of the film. The correlation is somewhat reduced upon annealing at about 900°C and for higher temperatures it is restored again. On the other hand vertical correlation of the interface roughness shows a significant increase towards the highest annealing temperatures. Upon annealing at lower temperatures, the structures of both films have relaxed slightly. This somewhat increases the correlation, especially in the vertical direction, as the contrast between two layers is getting more pronounced. The effect is not so apparent in the horizontal direction, since the early stage of clustering does not significantly affect changes in the SiO_x layer contrast. Still this can reduce the roughness of the SiO_x/SiO_2 interfaces of the layers, which influences more significantly the vertical correlation.

Higher temperature annealing introduces decomposition of SiO_x into SiO_2 + Si, according to formula:

$$SiO_x \rightarrow x/2SiO_2 + (1\text{-}x/2)Si \qquad (1)$$

see ref. [10], which inevitably destroys the correlation partly, and when Si particles begin to form, they somewhat enhance the scattering contrast and the correlation. Finally, at the highest temperature, both correlations are again slightly reduced .

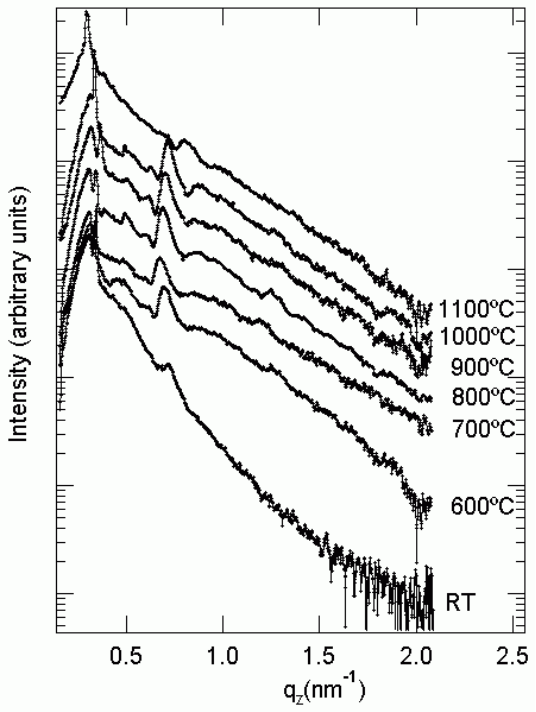

Figure 5 The scattering intensity in vertical direction taken at q_y=0.1 nm−1 from the 2D patterns vs. q_z and as a function of the annealing temperature. The curves are offset vertically for clarity.

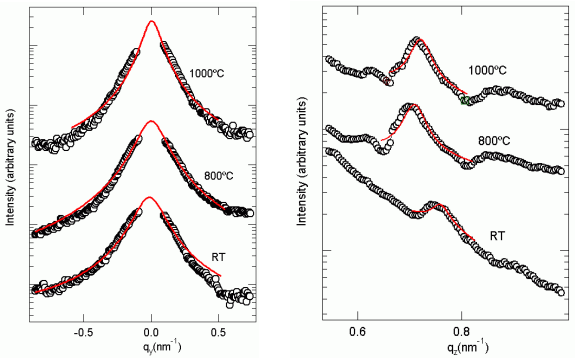

Figure 6 1D profiles across the Bragg peak taken along the horizontal (left panel) and vertical (right panel) plane, as indicated by white lines in Fig. 3., were extracted for the fitting procedure. The extracted 1D profiles (circles) and the corresponding fits (red lines) for the as-grown and annealed at 800°C and 1000°C films.

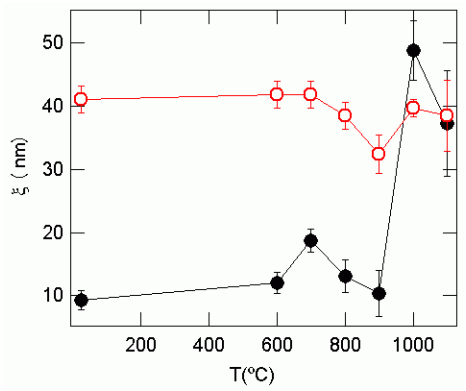

Figure 7 The horizontal (open red dots) and vertical (full black dots) correlation lengths obtained from the fitting as shown in Fig. 7. plotted vs. annealing temperature.

The subtraction of the surface signal from the scattering enhances the signal from the bulk, which includes also the multilayer scattering part. In order to analyze the particle signal, we extracted part of the signal away from the specular plain, where the surface contribution is minimized (the dashed line in Fig. 3.) An example of this signal is displayed in Fig. 8. where the scattering intensity is plotted as a function of the square of the wave vector (the Guinier plot). It can be shown [11] that the logarithm of the scattering intensity decays linearly with the square of the scattering angle, where the coefficient of regression is proportional to the size of the scattering object, regardless the shape, i.e.

$$\ln(I(q)) = \ln(I(0)) - \tfrac{1}{3}R_G^2 q^2 \qquad (2)$$

where I(q) is the scattering intensity at the given wave vector q, R_G is the radius of gyration of the charge distribution

$$R_G = \{\int \rho(r)\, r^2\, dV\} / \{\int \rho(r)\, dV\} \qquad (3)$$

Supposing that the particles are spheres of uniform density, the particles diameter can be deduced as

$$D = 2R_G\sqrt{(5/3)} \qquad (4)$$

The intensity plotted in Fig. 8. is approximated fairly well by a line, implying that there is a dominant, typical size, and the size distribution is relatively narrow. The deviation at q_z^2=0.5 nm^{-2} is the remaining contribution of the Bragg peak.

The obtained particles sizes D are plotted in Fig. 9. for the whole annealing temperature range, together with multilayer d-spacing (bilayer thickness) results obtained from the fits in Fig. 6. We can see that the bilayer thickness is peaked at 700ºC. The small increment at lower temperatures can be ascribed to structural annealing, while the minimum at the highest temperature is ascribed to SiO_x decomposition. The size of the detected inhomogeneities in the film is increasing slowly up to 800 – 900ºC, and there is a significant minimum at 1000ºC, which we ascribe to the onset of Si nanoparticle aggregation formation. The size of the particles is confined to 4-5 nm, justifying the role of the SiO_2 layers as a diffusion barrier. The particle signal, as it is, lacks the information about the particle to particle distance, and this is a result of poor ordering within the single layer. Also, the weakening of the Bragg peak intensity at the highest temperature shows that the particle to particle position correlation in vertical direction is stronger than that of the formed bilayers.

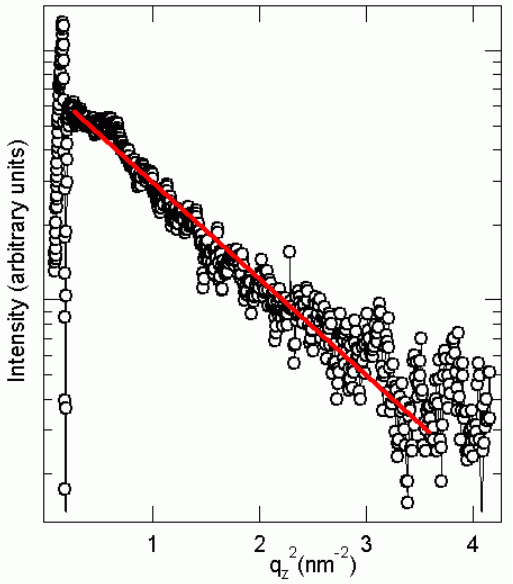

Figure 8 The Guinier plot taken from Fig. 3. at the position indicated by a white dashed line.

The results of GISAXS analysis are in a way model dependant and the difference in electronic density between Si clusters and/or nanoparticles and the SiO_2 matrix is only about 5% which renders therefore, a very low contrast difference. Therefore we support our GISAXS analysis by photoluminescence (PL) measurements shown in Fig. 10.

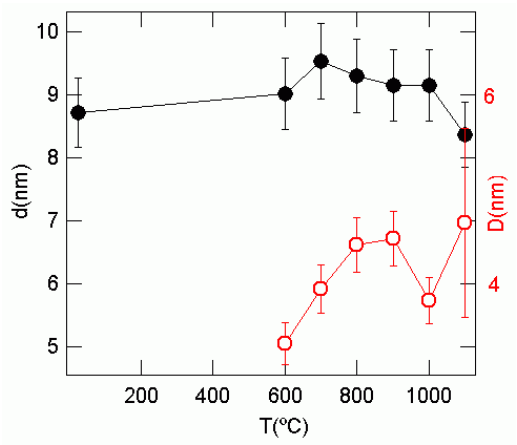

Figure 9 Thickness of the bilayers obtained from the peak position of the Bragg peak (obtained from Fig. 7.) and the diameter of the Si nanoparticles calculated from the Guinier plot illustrated in Fig. 8. Both parameters are plotted versus annealing temperature. Note the different scales.

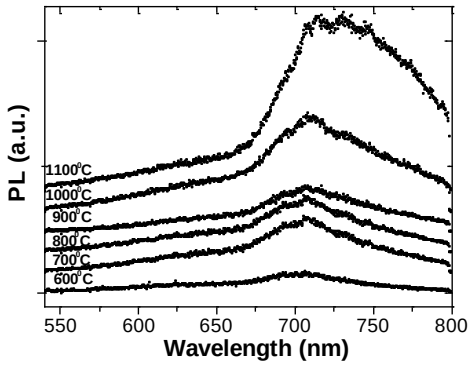

Figure 10 The photoluminescence spectra measured at room temperature of samples annealed between 600°C and 1100°C.

These PL results confirmed the existence of Si nanoparticles by the clear formation of peaks at about 700-730 nm upon high temperature annealing in vacuum, and hence our GISAXS results and the analysis [12]. Moreover, the size effects on the PL spectra taken at room temperature, as shown in ref. [13] confirms our GISAXS results about the diameter of Si nanoparticles.

4 Conclusions

SiO_x/SiO_2 superstructure was deposited by high vacuum evaporation from solid sources on Si substrate. Upon subsequent annealing Si nanoparticles were developed by thermal decomposition of SiO_x layers. The formed superstructure of Si nanoparticles embedded in SiO_2 matrix was thoroughly analysed by GISAXS spectroscopy with synchrotron light. Despite a very poor contrast difference between nanoparticles and the matrix we managed to prove the existence of the former. A method of removing the dominant surface scattering signal was explained as well as the detailed analysis of the contributions from the bulk. The results are supported by PL spectra that confirm our GISAXS analysis.

Acknowledgements This study has been partially funded by the MZOS of RH grants No. 098-0982886-2866, 098-0000000-2865 and by the EU project NanoPV (FP7-NMP3-SL-2011-246331).

References

[1] G. Conibeer et al., Thin Solid Films, **516**, 6748 (2008).
[2] L. Tsybeskov, K.D. Hirschman, S.P. Duttagupta, M. Zacharias, P.M. Fauchet, J.P. McCafrey, D.J. Lockwood, Appl. Phys. Lett **72**, 43 (1998).
[3] M. Zacharias, J. Heitman, R. Scholz, U. Kahler, M. Schmidt J. Blaesing, Appl. Phys. Lett. **80**, 661 (2002).
[4] I. Kovačević, P. Dubček. S. Duguay, H. Zorc, N. Radić, B. Pivac, A. Slaoui, S. Bernstorff, Physica E, **38**, 50 (2007).
[5] B. Pivac, P. Dubček, I. Capan, H. Zorc. S. Bernstorff, S. Duguay, A. Slaoui, Thin Solid Films, **516**, 6796 (2008).
[6] B. Pivac, P. Dubček, I. Capan, I. Zulim, T. Betti, H. Zorc, S. Bernstorff, J. Nanosci. Nanotechnol. **8**, 1 (2008).
[7] H. Amenitsch, S. Bernstorff, P. Laggner, Rev. Sci. Instrum. **66**, 1624 (1995).
[8] Y. Yoneda, Phys. Rev. 131, 2010 (1963)
[9] V. Holy, C. Giannini, L. Tapfer, T. Marschner, and W. Stolz, Pys. Rev. B **55**, 9960 (1997).
[10] B.J. Hinds, F. Wang, D.M. Wolfe, C.L. Hinkle, G. Lucovsky, J. Non-Cryst. Solids, **227-230**, 507 (1998).
[11] Guinier, A. & Fournet, G. (1955). *Small angle scattering of X-rays*, New York: Wiley.
[12] O. Jambois, H. Rinnert, X. Devaux, M. Vergnat, J. Appl. Phys. 98, 046105 (2005).
[13] Y. Kanemitsu and T. Kushida, Appl. Phys. Lett. **77**, 3550 (2000).